LETTER

Possible light–induced superconductivity in K_3C_{60} at high temperature

M. Mitrano[1], A. Cantaluppi[1,2], D. Nicoletti[1,2], S. Kaiser[1], A. Perucchi[3], S. Lupi[4], P. Di Pietro[3], D. Pontiroli[5], M. Riccò[5], S. R. Clark[1,6,7], D. Jaksch[7,8] & A. Cavalleri[1,2,7]

The non-equilibrium control of emergent phenomena in solids is an important research frontier, encompassing effects such as the optical enhancement of superconductivity[1]. Nonlinear excitation[2,3] of certain phonons in bilayer copper oxides was recently shown to induce superconducting-like optical properties at temperatures far greater than the superconducting transition temperature, T_c (refs 4–6). This effect was accompanied by the disruption of competing charge-density-wave correlations[7,8], which explained some but not all of the experimental results. Here we report a similar phenomenon in a very different compound, K_3C_{60}. By exciting metallic K_3C_{60} with mid-infrared optical pulses, we induce a large increase in carrier mobility, accompanied by the opening of a gap in the optical conductivity. These same signatures are observed at equilibrium when cooling metallic K_3C_{60} below T_c (20 kelvin). Although optical techniques alone cannot unequivocally identify non-equilibrium high-temperature superconductivity, we propose this as a possible explanation of our results.

Molecular solids of chemical formula A_3C_{60} often crystallize in face-centred cubic structures (Fig. 1a) in which each C_{60}^{3-} ion contributes three half-filled molecular orbitals to form narrow bands[9]. These electronic states give rise to superconductivity at equilibrium[10,11], mediated by a combination of electronic correlations[12,13] and local molecular vibrations[14–16].

In the experiments reported here, femtosecond mid-infrared optical pulses were used to excite K_3C_{60} powders (see Methods and Extended Data Fig. 1 for sample characterization). The excitation ('pump') pulses were tuned to wavelengths between 6 μm and 15 μm (200–80 meV photon energy), a spectral region in which both the metallic plasma and local molecular vibrations could be excited. The resulting changes in terahertz (THz)-frequency reflectivity and optical conductivity were measured with a second pulse (the 'probe'), a quasi-single-cycle THz-field transient, which was detected after reflection from the photo-excited material (see Methods and Extended Data Figs 2, 3). These transient changes were determined at different pump–probe time delays and normalized to the absolute equilibrium optical properties measured on the same sample (Extended Data Fig. 4).

Figure 1c displays two representative frequency-dependent equilibrium reflectivity spectra $R(\omega)$ measured above and below T_c (20 K). The corresponding real and imaginary part of the optical conductivity, $\sigma_1(\omega)$ and $\sigma_2(\omega)$, as extracted by Kramers–Kronig transformations, are shown respectively in Fig. 1d and e. Similar to what has been reported for K_3C_{60} single crystals[17–19], in the metallic state ($T = 25$ K) the optical conductivity displayed a narrow Drude peak and a polaronic band[20] centred at 55 meV. When cooling below T_c, a saturated reflectivity ($R = 1$), an optical gap in $\sigma_1(\omega)$ and a divergent $\sigma_2(\omega)$ emerged from the metal.

This equilibrium superconducting response is to be compared with that measured in metallic high-temperature K_3C_{60} after excitation

at 7 μm wavelength (180 meV photon energy), which is tuned to the $T_{1u}(4)$ vibration (see Fig. 2 for measurements at 1 ps time delay). For all temperatures between $T_c = 20$ K and $T = 100$ K, photo-excitation drove transient changes in the optical properties, which were very similar to those observed when cooling at equilibrium (see also Extended Data Fig. 5). At a 1 ps pump–probe time delay, we observed a saturated reflectivity ($R = 1$; Fig. 2a and d), gapped $\sigma_1(\omega)$ (Fig. 2b and e), and divergent $\sigma_2(\omega)$ (Fig. 2c and f).

Furthermore, all transient optical spectra could be fitted with the same function used for the low-temperature superconductor at equilibrium. An extension of the Mattis–Bardeen model was used, applicable to superconductors of arbitrary purity and taking into account both an optical gap (a superconducting component) and a fluid of normal quasi-particles (a Drude component)[21]. The non-equilibrium fits evidenced an 11 meV gap in the non-equilibrium $\sigma_1(\omega)$, nearly twice as large as the 6 meV superconducting gap at equilibrium.

Figure 3 reports similar measurements taken at higher temperatures, for which the effect progressively disappeared as temperature increased.
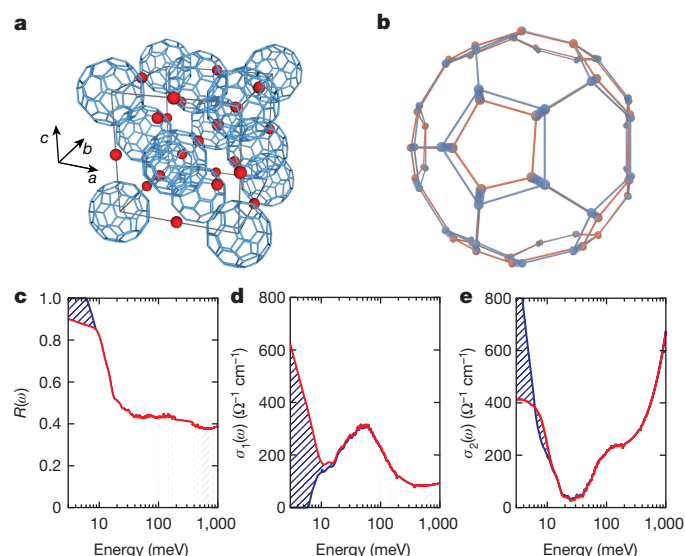

Figure 1 | Structure and equilibrium optical properties of K_3C_{60}.
a, Face-centred cubic (f.c.c.) unit cell of K_3C_{60} (ref. 26). Blue bonds link the C atoms in each C_{60} molecule. K atoms are represented as red spheres. **b**, C_{60} molecular distortion (red) along the $T_{1u}(4)$ vibrational mode coordinates. The equilibrium structure is displayed in blue. **c–e**, Equilibrium reflectivity at the sample–diamond interface $R(\omega)$ (**c**) and complex optical conductivity (**d**, real, $\sigma_1(\omega)$; **e**, imaginary, $\sigma_2(\omega)$) of K_3C_{60} measured at $T = 25$ K (red) and $T = 10$ K (blue). Hatched regions highlight changes across the superconducting transition.

[1]Max Planck Institute for the Structure and Dynamics of Matter, Luruper Chaussee 149, 22761 Hamburg, Germany. [2]The Hamburg Centre for Ultrafast Imaging, Luruper Chaussee 149, 22761 Hamburg, Germany. [3]INSTM UdR Trieste-ST and Elettra–Sincrotrone Trieste S.C.p.A., Area Science Park, 34012 Basovizza, Trieste, Italy. [4]CNR-IOM and Dipartimento di Fisica, Università di Roma "Sapienza", Piazzale A. Moro 2, 00185 Roma, Italy. [5]Dipartimento di Fisica e Scienze della Terra, Università degli Studi di Parma, Parco Area delle Scienze, 7/a, 43124 Parma, Italy. [6]Department of Physics, University of Bath, Claverton Down, Bath BA2 7AY, UK. [7]Department of Physics, Oxford University, Clarendon Laboratory, Parks Road, Oxford OX1 3PU, UK. [8]Centre for Quantum Technologies, National University of Singapore, 3 Science Drive 2, Singapore 117543, Singapore.
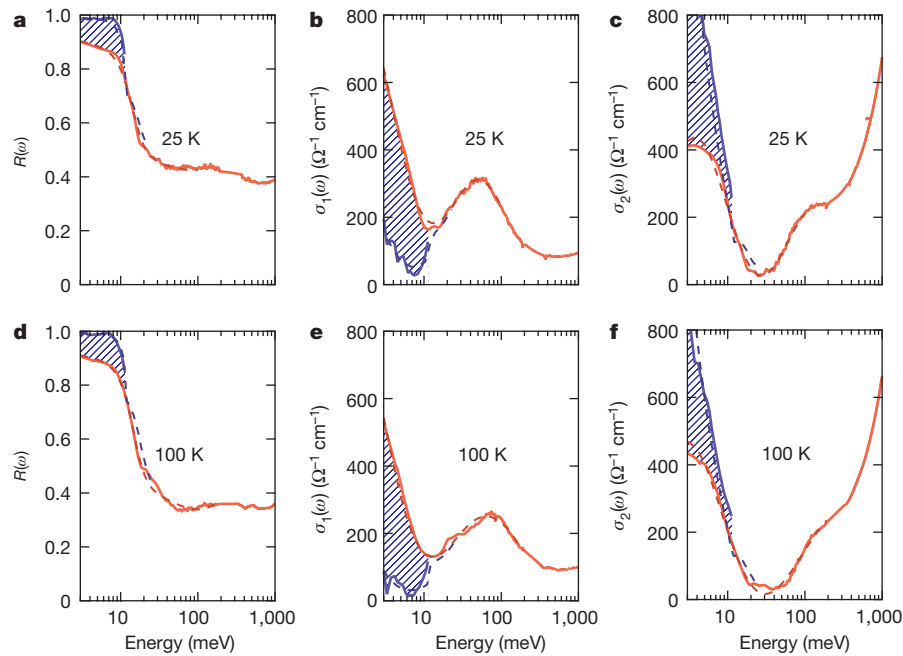
Figure 2 | Transient optical response of photo-excited K₃C₆₀ at T = 25 K and T = 100 K. Columns as Fig. 1; data taken at equilibrium (red) and 1 ps after photo-excitation (blue) at a pump fluence of 1.1 mJ cm⁻², measured at temperatures $T = 25$ K (**a–c**) and $T = 100$ K (**d–f**). Fits to the data are displayed as dashed lines. Hatched regions highlight pump-induced changes.

Only a partial reduction in $\sigma_1(\omega)$ and a less pronounced divergence in $\sigma_2(\omega)$ were observed. For these higher temperatures the Drude component alone was sufficient to fit the transient spectra, which did not exhibit a clear gap. However, we note that the $\sigma_1(\omega)$ Drude peak in the light-induced phase (blue curves in Fig. 3b and e) was always narrower than for the equilibrium metal (red curves in Fig. 3b and e), underscoring an optical enhancement in carrier mobility for all temperatures.

In Fig. 4, we plot the transient integrated loss in spectral weight (0.75–2.5 THz, that is, 3.1–10.3 meV) as a function of base temperature (Fig. 4a), pump–probe time delay (Fig. 4b), excitation fluence (Fig. 4c) and wavelength (Fig. 4d). The regions in which the optical properties required the full Mattis–Bardeen fit are shaded in blue, whereas those regions in which the fit yielded a gapless, Drude conductivity are shaded in white.

Figure 4a displays a crossover between a light-induced state with a Mattis–Bardeen gap (blue), observed up to $T = 100$ K, and a high-mobility metal (white) observed at higher temperatures. Similarly, in the time-delay dependence (Fig. 4b) a spectral-weight reduction was observed immediately after the excitation pulse (red curve), followed by a gap opening only at later time delays (blue shading). The gapped state disappeared after approximately 2 ps, and the rest of the decay involved relaxation of a high-mobility metal (white shading) with an exponential time constant of ~10 ps (see Extended Data Fig. 6 for representative spectra as a function of pump–probe delay).
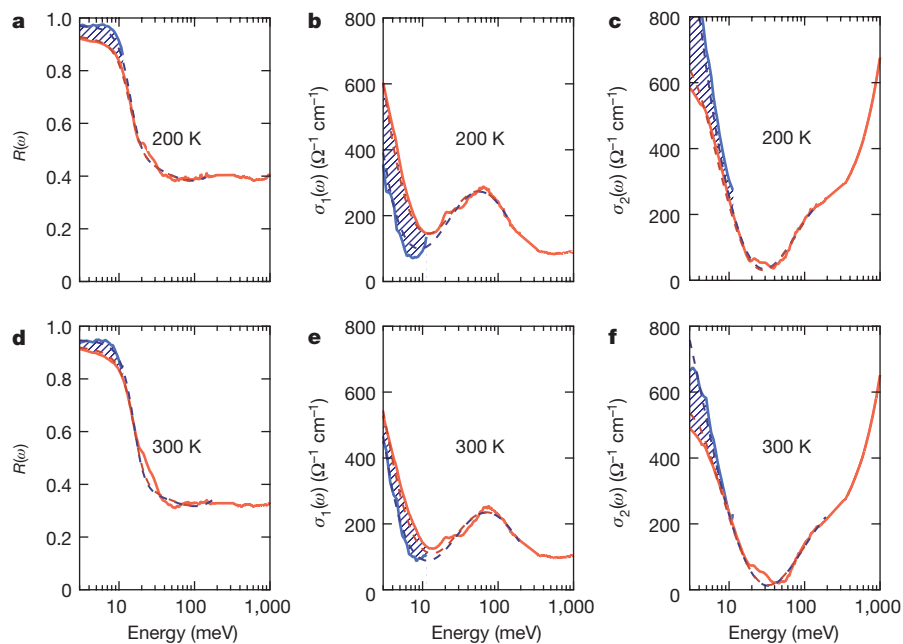

Figure 3 | Transient optical response of photo-excited K₃C₆₀ at T = 200 K and T = 300 K. Columns as Fig. 1; data taken at equilibrium (red) and 1 ps after photo-excitation (blue) with a pump fluence of 1.1 mJ cm⁻², measured at temperatures $T = 200$ K (**a–c**) and $T = 300$ K (**d–f**). Fits to the data are displayed as dashed lines. Hatched regions highlight pump-induced changes.
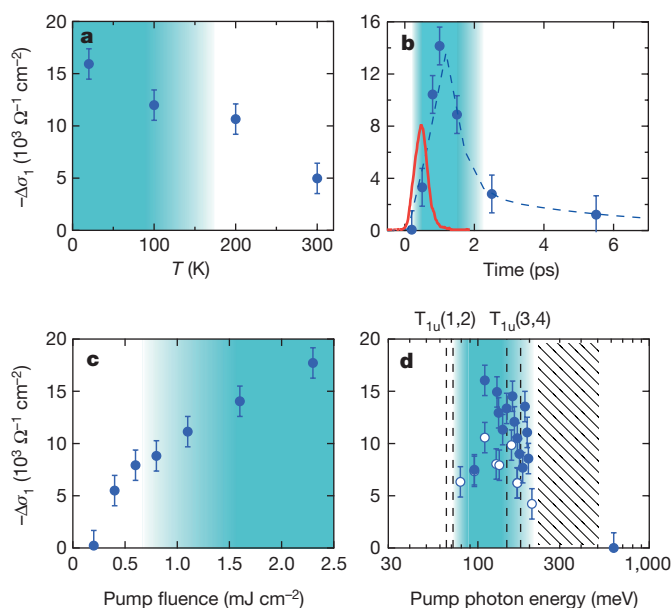
Figure 4 | Scaling of the $\sigma_1(\omega)$ gap with experimental parameters.
In all panels, the photo-induced reduction in $\sigma_1(\omega)$ spectral weight,
$-\Delta\sigma_1$, integrated between 0.75 THz and 2.5 THz, is plotted on the
y axis (represented by filled circles). **a–d**, The lost spectral weight is plotted
as a function of temperature (**a**), pump–probe time delay (**b**), pump
fluence (**c**) and pump wavelength (**d**). Error bars represent maximum
uncertainties determined from different sets of measurements. The regions
shaded in blue indicate the parameter ranges for which the transient
response was fitted with a model for a superconductor. The red curve in **b**
is the pump pulse profile (cross-correlation signal), while the dashed line
is a double exponential fit ($\tau_1 \approx 1$ ps, $\tau_2 \approx 10$ ps). Dashed vertical lines in **d**
are the frequencies of the four T_{1u} vibrational modes. The experiments
were not possible for pump wavelengths between 6 μm and 3 μm (hatched
region in **d**) owing to absorption in the diamond window that contained
the K_3C_{60} powders. White and blue filled circles are data taken at fluence
values of 0.4 mJ cm^{-2} and 1.1 mJ cm^{-2}, respectively. Data in **b–d** were
measured at $T = 25$ K.

The pump fluence dependence of Fig. 4c reveals a similar crossover.
Metallic conductivities (white) were observed for low excitation levels
($F \lesssim 0.8$ mJ cm^{-2}), whereas fully gapped states (blue) emerged only at
higher fluences ($F \gtrsim 0.8$ mJ cm^{-2}).

Finally, when tuning the pump to short wavelengths (2 μm, 620 meV
photon energy) no response was found (Fig. 4d). On the contrary,
a strong response was measured when the pump was made resonant
with the $T_{1u}(4)$ and $T_{1u}(3)$ modes, which correspond both to stretching
and compressing of the hexagons and pentagons of the fullerene mole-
cule (see Fig. 1b). A weaker response was still observed for wavelengths
extending towards the $T_{1u}(2)$ and $T_{1u}(1)$ resonances.

One possible interpretation for the data above posits that excitation
of molecular vibrations can coherently stimulate a transition from the
high-temperature metallic state into a non-equilibrium superconduct-
ing phase.

To first order, T_{1u} vibrations do not couple to the t_{1u} electronic states
that cross the Fermi level, because $T_{1u} \neq t_{1u} \times t_{1u}$. However, for the
strong optical fields used here (~ 1.5 MV cm^{-1}), and from the polar-
izability of the T_{1u} molecular vibrations, we estimate large oscillatory
distortions of the C–C bonds amounting to several per cent of their
equilibrium bond lengths. Hence, the large amplitude excitation is
expected to extend beyond a linear response, and to deform the struc-
ture of the solid along other, anharmonically coupled coordinates. To
lowest order, these couplings are described by $q_{T_{1u}}^2 Q$ terms in the non-
linear lattice Hamiltonian[2,22,23], where $q_{T_{1u}}$ is the directly driven mode
coordinate, and Q is the coordinate of any distortion contained in the
irreducible representation of $T_{1u} \times T_{1u}$.

As discussed in the Methods section, excitation of the T_{1u} molecular
mode is expected to drive a sizeable distortion along normal mode
coordinates of H_g symmetry. Because H_g modes are thought to assist
pairing at equilibrium[9], it is possible that a quasi-static H_g molecular
deformation might favour stronger superconductivity, for example by
causing an increase in the electron–phonon coupling (see Extended
Data Fig. 7).

Excitation of T_{1u} vibrations is also expected to modulate local
electronic correlations. For a molecular mode of coordinate q_{IR} with
classical vibrational coordinate $q_{IR}(\tau) = C\sin(\Omega_{IR}\tau)$, where C is a pro-
portionality constant, Ω_{IR} is the driving frequency and τ the time delay,
we expect the charge density on each molecule to 'slosh' backwards and
forwards[24]. Deformation of the molecular orbital causes a modification
of the Coulomb repulsion U_a for the t_{1u} orbital ($a = \{x, y, z,\}$), which
can be written as $U_a(\tau) = U_a + \Delta U_a(1 - \cos(2\Omega_{IR}\tau))$. This highlights
two effects: a modulation of the onsite Coulomb integral at twice the
frequency of the driven molecular mode, and an average change in
correlation energy, ΔU_a, which have both been observed in a different
organic compound[25].

Although a complete quantitative analysis requires a dynamical
quantum chemistry calculation, an order-of-magnitude estimate for
these changes in local electronic correlations can be extracted from
frozen atomic motions for the $T_{1u}(4)$ mode. This estimate predicts a
change in electronic repulsion ΔU_a as high as $\sim 10\%$ of the equilibrium
correlation energy for the orbitals orthogonal to the vibrational polar-
ization (see Methods and Extended Data Fig. 8). Such a large asym-
metric increase in U_a for only one orbital unbalances the occupancy
of the three t_{1u} orbitals. This effect may interact with the dynamical
Jahn–Teller coupling known to contribute to superconductivity near
equilibrium[9].

However, the interpretation of the data proposed above is not unique.
First, some other transient non-superconducting states would also be
consistent with the optical properties revealed by our experiments.
A large reduction in carrier scattering rate without condensation may
be sufficient to explain these results. The measured gap in the transient
conductivity would then simply emerge from the equilibrium polaronic
band at 55 meV as the broad Drude absorption narrows. However, this
scenario is difficult to reconcile with the estimated increase, rather than
decrease, of the carrier effective mass (see Methods). Alternatively, one
may also consider a sliding, non-commensurate charge density wave,
which would be promoted by the enhanced electron–phonon coupling.

Second, the mid-infrared pulses used to excite the sample couple not
only to the vibrations but also to the metallic plasma. The measured
photo-conductivity signal exhibits a peak in the region of the molecular
vibrations (Fig. 4d), but this peak appears broadened compared to the
mode linewidths. This might be an indication that a modulation of the
local charge density also plays a role in driving the photo-induced state.

Other observations, not mentioned above, appear important but are
not well understood. The light-induced high-mobility phase is only
induced for temperatures above, but not below, $T_c = 20$ K. Unlike in
the case of light-enhanced superconductivity in the cuprates, in which
excitation of a phonon below T_c caused a stiffening of the Josephson
plasma resonance[4], in the present case we did not observe any widen-
ing of the equilibrium superconducting gap at temperatures below T_c.
Rather, we measured very little perturbation at the same pump–probe
delay (1 ps) for which the response above T_c was maximum (Extended
Data Fig. 9), followed by a filling in of the gap by hot quasi-particles at
later time delays (Extended Data Fig. 10). This suggests that the equi-
librium superconductor and the high-mobility transient state compete
with one another. One may rationalize this observation by hypo-
thesizing that equilibrium superconductivity depletes states near the
Fermi level, which then cannot participate in the formation of the non-
equilibrium state when stimulated by the light.

On balance, although a definitive assignment should rest on further
experimentation and theoretical analysis, we favour an interpretation
based on stimulated superconductivity. However, the data above are

indicative of striking emergent physics away from equilibrium regard-less of the specific mechanism, and provide many new opportunities and challenges for both theory and experiments.

1. Fausti, D. et al. Light-induced superconductivity in a stripe-ordered cuprate. Science **331,** 189–191 (2011).
2. Mankowsky, R. et al. Nonlinear lattice dynamics as a basis for enhanced superconductivity in YBa$_2$Cu$_3$O$_{6.5}$. Nature **516,** 71–73 (2014).
3. Mankowsky, R. et al. Coherent modulation of the YBa$_2$Cu$_3$O$_{6+x}$ atomic structure by displacive stimulated ionic Raman scattering. Phys. Rev. B **91,** 094308 (2015).
4. Kaiser, S. et al. Optically-induced coherent transport far above T_c in underdoped YBa$_2$Cu$_3$O$_{6+\delta}$. Phys. Rev. B **89,** 184516 (2014).
5. Hu, W. et al. Optically enhanced coherent transport in YBa$_2$Cu$_3$O$_{6.5}$ by ultrafast redistribution of interlayer coupling. Nature Mater. **13,** 705–711 (2014).
6. Hunt, C. R. et al. Two distinct kinetic regimes in the relaxation of light induced superconductivity in La$_{1.675}$Eu$_{0.2}$Sr$_{0.125}$CuO$_4$. Phys. Rev. B **91,** 020505 (2015).
7. Först, M. et al. Melting of charge stripes in vibrationally driven La$_{1.875}$Ba$_{0.125}$CuO$_4$: assessing the respective roles of electronic and lattice order in frustrated superconductors. Phys. Rev. Lett. **112,** 157002 (2014).
8. Först, M. et al. Femtosecond X-rays link melting of charge density wave correlations and light enhanced coherent transport in YBa$_2$Cu$_3$O$_{6.6}$. Phys. Rev. B **90,** 184514 (2014).
9. Gunnarsson, O. Alkali-doped Fullerides: Narrow-band Solids with Unusual Properties (World Scientific, 2004).
10. Hebard, A. F. et al. Superconductivity at 18 K in potassium-doped C$_{60}$. Nature **350,** 600–601 (1991).
11. Xiang, X.-D. et al. Synthesis and electronic transport of single crystal K$_3$C$_{60}$. Science **256,** 1190–1191 (1992).
12. Chakravarty, S., Gelfand, M. P. & Kivelson, S. Electronic correlation effects and superconductivity in doped fullerenes. Science **254,** 970–974 (1991).
13. Capone, M. et al. Strongly correlated superconductivity. Science **296,** 2364–2366 (2002).
14. Varma, C. M., Zaanen, J. & Raghavachari, K. Superconductivity in the fullerenes. Science **254,** 989–992 (1991).
15. Schluter, M. et al. Electron-phonon coupling and superconductivity in alkali-intercalated C$_{60}$ solid. Phys. Rev. Lett. **68,** 526–529 (1992).
16. Han, J. E., Gunnarson, O. & Crespi, V. H. Strong superconductivity with local Jahn Teller phonons in C$_{60}$ solids. Phys. Rev. Lett. **90,** 167006 (2003).
17. Degiorgi, L. et al. Optical properties of the alkali-metal-doped superconducting fullerenes: K$_3$C$_{60}$ and Rb$_3$C$_{60}$. Phys. Rev. B **49,** 7012–7025 (1994).
18. Degiorgi, L. et al. Optical measurements of the superconducting gap in single-crystal K$_3$C$_{60}$ and Rb$_3$C$_{60}$. Nature **369,** 541–543 (1994).
19. Degiorgi, L. The complete excitation spectrum of the alkali-metal-doped superconducting fullerenes. Mod. Phys. Lett. B **9,** 445–468 (1995).
20. Rice, M. G. & Choi, H.-Y. Charged-phonon absorption in doped C$_{60}$. Phys. Rev. B **45,** 10173–10176 (1992).
21. Zimmermann, W. et al. Optical conductivity of BCS superconductors with arbitrary purity. Physica C **183,** 99–104 (1991).
22. Först, M. et al. Nonlinear phononics as a new ultrafast route to lattice control. Nature Phys. **7,** 854–856 (2011).
23. Subedi, A., Cavalleri, A. & Georges A. Theory of nonlinear phononics for coherent light control of solids. Phys. Rev. B **89,** 220301(R) (2014).
24. Kaiser, S. et al. Optical properties of a vibrationally modulated solid state Mott insulator. Sci. Rep. **4,** 3823 (2014).
25. Singla, R. et al. THz-frequency modulation of the Hubbard U in an organic Mott insulator. Phys. Rev. Lett. **115,** 187401 (2015).
26. Stephens, P. W. et al. Structure of single-phase superconducting K$_3$C$_{60}$. Nature **351,** 632–634 (1991).

Author Contributions A. Cavalleri conceived the project and the experiments together with M.M. and S.K. The time-resolved THz set-up was built by M.M. and A. Cantaluppi, who performed the pump–probe measurements and analysed the data with support from D.N. and S.K. Equilibrium optical properties were measured and analysed by M.M. and A. Cantaluppi, with support from A.P., S.L. and P.D.P. Samples were grown and characterized by D.P. and M.R. S.R.C. and D.J. provided calculations of time-dependent on-site correlation energies. The manuscript was written by A. Cavalleri, D.N. and M.M., with input from all authors.

METHODS

Sample growth and characterization. Stoichiometric amounts of finely ground C_{60} powder and potassium metal were sealed in a cylindrical vessel and closed in a Pyrex vial under vacuum ($\sim 10^{-6}$ torr). The potassium was kept separated from the fullerene powder during the thermal treatment, therefore only potassium vapour came in contact with C_{60}. The two reagents were heated at 523 K for 72 h and then at 623 K for 28 h. The vessel was then opened and the recovered black powder was reground and pelletized. Afterwards, the pellets were further annealed at 623 K for 5 days. All described operations were performed in inert atmosphere (vacuum or Ar glove box with <0.1 p.p.m. O_2 and H_2O). The final product, K_3C_{60}, was characterized by laboratory powder X-ray diffraction and SQUID magnetometry (Extended Data Fig. 1).

Equilibrium optical properties and fitting models. The K_3C_{60} equilibrium optical response was measured on compacted powder pellets (100–400 nm average grain size) sealed in a custom sample holder and pressed against a diamond window, ensuring an optically flat interface.

Broadband infrared reflectivity measurements were carried out at the SISSI beamline (Elettra Synchrotron Facility, Trieste)[27]. The sample was mounted on a cryostat coupled to a Bruker Vertex70 interferometer through a Hyperion microscope. The sample temperature was varied between 300 K and 25 K. The spectra were referenced against the reflectivity of a gold mirror placed into the holder at the sample position.

Data below 3 meV have been extrapolated with the Hagen–Rubens formula, while at high frequency the recalculated sample–diamond reflectivity from single crystal data was used[18]. The complex optical conductivity was determined through a Kramers–Kronig algorithm for samples in contact with a transparent window[28].

All spectra at $T > T_c$ are reported in Extended Data Fig. 4a. The low energy ($\lesssim 200$ meV) part of the complex conductivity was fitted at all $T > T_c$ with a Drude term and a Lorentz oscillator, which reproduced the polaronic absorption centred at ~ 55 meV (ref. 17; a representative fit to the 25 K data is also displayed).

The sample reflectivity in the superconducting state was determined as follows. We first measured the reflected electric field at different $T < T_c$ using THz time-domain spectroscopy. Each spectrum was then referenced against the reflected field at 25 K, for which the broadband reflectivity was known from the synchrotron measurements.

In Extended Data Fig. 4b the reflectivity measured at different $T < T_c$ is shown. The data were extrapolated below 3 meV using the Zimmermann model[21], a generalization of the Mattis–Bardeen optical conductivity for BCS superconductors with arbitrary purity. The optical conductivity was determined through the same Kramers–Kronig procedure described above. The real and imaginary conductivities are also reported in Extended Data Fig. 4b.

The gap opening in $\sigma_1(\omega)$ and the $1/\omega$ divergence in $\sigma_2(\omega)$ observed upon cooling below T_c are indicative of the superconducting transition. Through fits to the data performed with the Zimmermann model[21], the optical gap 2Δ could be determined as a function of temperature. Both its zero temperature value $2\Delta(T=0) \approx 6$ meV and temperature dependence $2\Delta(T)$—closely following the mean field prediction—were found to be in full agreement with previously published data on K_3C_{60} single crystals[18], as shown in Extended Data Fig. 4b inset.

In Extended Data Fig. 4c, d we show a direct comparison of the equilibrium optical properties (below and above T_c) measured on our K_3C_{60} powders with those reported for single crystals[18]. First, we observe that the polaronic absorption at ~ 55 meV maintains the very same shape and central frequency. Second, the effect that the superconducting transition has on the low-frequency optical properties in our K_3C_{60} powder is identical to that measured in the single crystals, which exhibit the same $T_c \approx 20$ K and the same optical gap $2\Delta(T=0) \approx 6$ meV.

The only difference between the single crystal data and the present measurements is in the carrier density and scattering rate. As is well known for this class of materials[19], in powdered samples both these quantities can be different from those of a single crystal. From Drude–Lorentz fits to the data, we could estimate a reduction of a factor of ~ 4 in carrier density n (the Drude plasma frequency $\omega_p \propto \sqrt{n}$ reduces from $\omega_p^{crystal} \approx 410$ meV to $\omega_p^{powder} \approx 175$ meV) and of a factor of ~ 4 in the scattering rate (from $\Gamma^{crystal} \approx 18$ meV to $\Gamma^{powder} \approx 4$ meV).

Also the spectral weight Ω_{pol}^2 of the 55 meV polaronic band is a factor of ~ 4 higher in the single crystal ($\Omega_{pol}^{crystal} \approx 1{,}100$ meV against $\Omega_{pol}^{powder} \approx 540$ meV). This implies that the quantity $\omega_p^2 / \Omega_{pol}^2$ extracted for our sample is very close to that reported in ref. 17, thus indicating that the relative ratio between mobile and localized carriers is the same in powders and single crystals.

Determination of the transient optical properties. THz-frequency probe pulses, generated by optical rectification of 800 nm pulses in a ZnTe crystal, were used to measure the transient response of the sample after excitation. These probe pulses were detected after reflection from the sample–diamond interface in a

second ZnTe crystal, yielding pump-induced reflectivity changes for frequencies between 0.75 THz and 2.5 THz (3.1–10.3 meV) and with a pump–probe time-delay resolution of approximately 300 fs.

The pump-induced change in the THz electric field $\Delta E_R(t, \tau) = E_R^{pumped}(t, \tau) - E_R(t)$ was acquired at each time delay τ by filtering the electro-optic sampling signal with a lock-in amplifier, triggered by modulation of the mid-infrared pump with a mechanical chopper. This measurement yielded 'pump on' minus 'pump off' reflected electric field.

The differential electric field $\Delta E_R(t, \tau)$ and the stationary reflected electric field $E_R(t)$ were independently Fourier transformed to obtain the complex-valued, frequency dependent $\Delta \widetilde{E}_R(\omega, \tau)$ and $\widetilde{E}_R(\omega)$.

Importantly, because the pump-induced changes were large ($\sim 2\%$), the same measurement was repeated by directly recording $\widetilde{E}_R^{pumped}(\omega, \tau)$ and $\widetilde{E}_R(\omega)$ without chopping the pump, and then calculating $\Delta \widetilde{E}_R(\omega, \tau) = \widetilde{E}_R^{pumped}(\omega, \tau) - \widetilde{E}_R(\omega)$. This method does not require calibration of the absolute phase of the lock-in amplifier, and avoids phase errors in estimating the optical properties. The two methods yielded identical results.

In Extended Data Fig. 2, $E_R(t)$ and $\Delta E_R(t, \tau > 0)$ are displayed both below and above T_c with the corresponding normalized reflectivity changes. For all measured $T > T_c$ and for any $\tau > 0$, all $\Delta E_R(t, \tau)$ and $E_R(t)$ have the same phase, indicating that above T_c one always finds an increase in reflectivity. On the other hand, all measurements below T_c exhibit an opposite phase, that is, reflectivity is reduced upon excitation.

The complex reflection coefficient of the photo-excited material, $\tilde{r}(\omega, \tau)$, was determined using the relation

$$\frac{\Delta \widetilde{E}_R(\omega, \tau)}{\widetilde{E}_R(\omega)} = \frac{\tilde{r}(\omega, \tau) - \tilde{r}_0(\omega)}{\tilde{r}_0(\omega)}$$

To calculate these ratios, the stationary reflection coefficient $\tilde{r}_0(\omega)$ was extracted at all temperatures from the equilibrium optical properties, determined independently (at the same temperature and in the same sample holder) with synchrotron-based infrared spectroscopy.

These 'raw' light-induced changes, which indicate increase and decrease of the reflectivity above and below T_c, respectively, were reprocessed to take into account the penetration depth mismatch between THz probe ($L \approx 700$–800 nm) and mid-infrared pump ($d \approx 200$ nm) (Extended Data Fig. 3a). Importantly, this renormalization only affects the size of the response, whereas the qualitative change in optical properties is independent of it and of the specific model chosen.

As in, for example, ref. 1, this mismatch can be taken into account most simply by modelling the response of the system as that of a homogeneously photo-excited layer with the unperturbed bulk beneath it (Extended Data Fig. 3b). However, this model applies well only in case of large pump–probe penetration depth mismatches ($d/L \approx 10^2$–10^3).

A more precise method consists of treating the excited surface as a stack of thin layers with a homogeneous refractive index, and describing the excitation profile by an exponential decay[4] (see Extended Data Fig. 3c). By calculating the coupled Fresnel equations of such a multi-layer system, the refractive index at the surface, $\tilde{n}(\omega, \tau)$, can be retrieved, and from this the complex conductivity for a volume that is homogeneously transformed:

$$\tilde{\sigma}(\omega, \tau) = \frac{\omega}{4\pi i}[\tilde{n}(\omega, \tau)^2 - \varepsilon_\infty]$$

In Extended Data Fig. 3d–f we compare the transient optical properties obtained with the exponential decay model (same curves as in Fig. 2a–c) with those obtained with the single-layer description (having used the same pump penetration depth $d = 220$ nm). Both treatments yield very similar results, although we consider the exponential model more accurate.

Note that the extracted optical properties from pump–probe data can sometimes be affected at the earliest time delays by perturbed free induction decay[29]. This issue was raised recently in discussing transient THz probing of superconductors[30]. However, this effect occurs only when coherence is transiently induced on a time-scale far shorter than the momentum relaxation time and the response time of the detector[31]. Here the excitation of the transient high-mobility state is achieved with 300 fs mid-infrared pulses, the rise time of the signal is 1 ps, and the relaxation occurs within 2–10 ps. Therefore these effects are negligible[32].

Comparing transient conductivities below and above T_c. Transient optical properties above and below T_c measured at the same time delay after photo-excitation are shown in Extended Data Fig. 9 ($\tau = 1$ ps, same above-T_c data as in Fig. 2a–c).

Importantly, although the equilibrium properties of the unperturbed solid are very different (normal and superconducting state, red and blue curves in Extended

Data Fig. 9a–c and d–f, respectively), the two light-induced states are quite similar to one another (light blue curves). In both cases, the state at $\tau = 1$ ps after excitation is gapped.

As shown in Extended Data Fig. 2, these transient properties derive in one case ($T > T_c$) from a light-induced increase in reflectivity (which saturates to $R \approx 1$ at $\omega < 2\Delta$), while in the other case ($T < T_c$), from a decrease in reflectivity (partial gap filling).

The relaxation dynamics of these two states towards equilibrium are shown in Extended Data Figs 6, 10. Above T_c, the gapped state measured at $\tau = 1$ ps rapidly relaxes into a state with a gapless optical conductivity. The metallic ground state is then recovered within ~5 ps. Below T_c, after the early time response shown in Extended Data Fig. 9, at $\tau = 3$ ps the conductivity gap becomes filled. The superconducting ground state is then recovered over relatively long timescales (>20 ps).

Uncertainties in determining the transient optical properties. We examine here different sources of uncertainty and their propagation. The uncertainty in the absolute value of the measured equilibrium reflectivity is of the order of $\pm 1\%$. Extended Data Fig. 5a shows as coloured bands the propagated error bars in the equilibrium and transient optical properties for a $\pm 1\%$ and a larger $\pm 2.5\%$ uncertainty in $R(\omega)$. In both cases the response remains gapped.

We next examine uncertainty in the Fresnel phase coefficient β, used in the Kramers–Kronig transformations. This has been set to $\beta = 217$ meV to precisely match the central frequency of the polaronic band (55 meV) with that reported in previous optical studies[17,18] on the same compound. In Extended Data Fig. 5b we show how a $\pm 10\%$ uncertainty in β would affect the equilibrium and transient optical response.

Another possible source of error resides in the pump penetration depth value used to retrieve the transient reflectivities and optical conductivities. This value was set to $d = 220$ nm for all analysed data. In Extended Data Fig. 5c we show how a $\pm 25\%$ change in d would affect the transient optical properties.

Finally, in Extended Data Fig. 5d we show the effect of a different choice of functional form for the decay of $\tilde{n}(\omega, z)$ in the multi-layer model. The exponential decay used for all data analysed in the paper is compared with a single layer (already introduced above) and with a Gaussian-like decay, all having the same d value.

In all these cases the impact of the different sources of error on the calculated reflectivities and optical conductivities is moderate and the qualitative behaviour of the spectra is not affected.

Estimate of the carbon atom displacement. The peak electric field of the mid-infrared pulses can be estimated from

$$E = \sqrt{\frac{F}{2\varepsilon_0 c \Delta t}}$$

where c is the speed of light, ε_0 is the vacuum permittivity and Δt is the pulse duration. The fluence F typically used in these experiments is 1 mJ cm^{-2}, which, for a pulse duration of approximately 300 fs, corresponds to a peak electric field $E = 800$ kV cm^{-1}.

From previous optical measurements[33], it is known that the real part of the optical conductivity on the pumped $T_{1u}(4)$ phonon is $\sigma_1[T_{1u}(4)] = 120 \, \Omega^{-1}$ cm^{-1}, while its central frequency is $\omega_0 = 168.62$ meV. The pump-induced polarization P (in units of C cm^{-2}) is then given by

$$P = \frac{\sigma_1(\omega_0)}{\omega_0} E = 2.35 \times 10^{-6}$$

The polarization arises owing to a light-induced dipole moment $P = n \delta Z_{\text{eff}} e$, where n is the number of dipoles per unit volume, $Z_{\text{eff}} e$ is the effective charge defined as in ref. 34 and δ is the atomic displacement. The Z_{eff} determined for this vibration is 0.147. Under the assumption that all the incident photons are contributing to the excitation, one can estimate from the polarizability a displacement $\delta = 0.24$ Å, that is, approximately 17% of the C–C bond length.

Mode coupling and electronic structure calculations. Electronic structure, lattice dynamics, and nonlinear phonon couplings after excitation of the $T_{1u}(4)$ phonon were obtained using density functional theory (DFT) calculations with a plane-wave basis set and projector augmented wave pseudopotentials (VASP software package)[35]. These calculations were performed within the local density approximation (LDA) with a 900 eV cut-off for the plane-wave basis set. A $6 \times 6 \times 6$ k-point grid and a 0.1 eV Gaussian smearing were used for the Brillouin-zone integration during the self-consistency cycles. Lattice parameters and atomic positions were obtained by energy minimization, ignoring the C$_{60}$ orientational disorder. The calculated lattice constant is 13.888 Å, in good agreement with the experimental value of 14.240 Å.

Phonon frequencies and eigenvectors were determined using the frozen-phonon approach (as implemented in the PHONOPY software package)[36]. After the normal modes were identified, total energy curves as a function of the Raman

mode amplitude Q were calculated while simultaneously keeping the amplitude of the pumped $T_{1u}(4)$ mode finite. A shift of the Raman mode energy minimum for finite amplitude of the $T_{1u}(4)$ vibration allowed to identify a cubic $q_{T1u}^2 Q$ coupling between the pumped infrared mode and the Raman vibration (see Extended Data Fig. 7a).

Electron–phonon calculations were performed using DFT-LDA (as implemented in the Quantum ESPRESSO software package)[37] with 42 Ry and 420 Ry cut-offs for the plane-wave basis set and the charge-density expansions, respectively. A $6 \times 6 \times 6$ k-point grid and a 0.020 Ry Gaussian smearing were used for Brillouin-zone integration during the self-consistency cycles.

The majority of Raman modes couple to the $T_{1u}(4)$ mode. In Extended Data Fig. 7a we show the shift in the $H_g(1)$ mode minimum when the amplitude of the $T_{1u}(4)$ mode is 2.0 Å $\sqrt{\text{amu}}$. Such a shift implies that the structure is displaced along the $H_g(1)$ coordinate while the $T_{1u}(4)$ mode is pumped. We also report the band structure, electronic density of states (Extended Data Fig. 7b), and electron–phonon coupling (Extended Data Fig. 7c) for a structure displaced along the $H_g(1)$ coordinate with an amplitude of 1.5 Å $\sqrt{\text{amu}}$. We find that such displacement slightly lifts the degeneracy of the t_{1u} states. However, these bands remain part of a single manifold, crossing each other at various points along the high-symmetry path of the Brillouin zone.

We also find a modest change in the density of states, which is caused by the shift of a van Hove singularity near Γ as the bands are moved by the $H_g(1)$ mode displacement. Furthermore, the bandwidth of the t_{1u} manifold steadily increases as a function of $H_g(1)$ mode amplitude. This is reasonable, since the $H_g(1)$ displacements elongate the C$_{60}$ molecule and reduce the intermolecular distances, thus increasing the intermolecular hopping.

The $H_g(1)$ displaced structure develops strong coupling between electrons and intermolecular phonon modes (Extended Data Fig. 7c). At equilibrium the three intermolecular modes with 5 meV energy do not couple to the t_{1u} electrons, while under displacement along the $H_g(1)$ coordinate two of these modes exhibit very large electron–phonon coupling.

The electron–phonon coupling, obtained by integrating the Eliashberg function $\alpha^2 F(\omega)$, is 0.52 at equilibrium and 1.44 for the $H_g(1)$ displaced structure. Energy-resolved changes in the electron–phonon coupling function, evaluated as $\Delta \alpha^2 F(\omega) = \alpha^2 F(\omega)_{H_g(1)} - \alpha^2 F(\omega)_{\text{equilibrium}}$, are reported in Extended Data Fig. 7d. The increased coupling at low energy and a strong reshaping at high frequency (>130 meV) are apparent.

Time-dependent onsite correlation energies. We estimated the magnitude of changes to the inter- and intra-orbital Coulomb repulsion of the t_{1u} orbitals on a single C$_{60}$ molecule when the $T_{1u}(4)$ vibrational mode is driven. The relevant C$_{60}$ molecular orbitals are described by pπ orbitals projecting radially outwards at each C atom. A tight-binding Hückel model captures the hybridization of these orbitals in the C$_{60}$ cage. Hopping amplitudes are assumed to vary with the distance d between C atoms as

$$V(d) = \frac{\Lambda}{d^2} \quad (1)$$

where $\Lambda = 5.63$ eV Å^2. We take the C–C and C=C bond lengths as $d_S = 1.45$ Å and $d_D = 1.37$ Å, corresponding to $V_S = 2.69$ eV and $V_D = 3.00$ eV hopping integrals for the pentagonal-hexagonal and hexagonal-hexagonal edges of the C$_{60}$ cage. The x, y and z t_{1u} orbitals are the degenerate 31st to 33rd single electron eigenstates of the Hückel model and the lowest unoccupied molecular orbitals of free C$_{60}$ (ref. 38). In Extended Data Fig. 8a, the wavefunction (chosen to be real) for each t_{1u} orbital is plotted over the buckyball with the size of the spheres denoting the magnitude and the colour denoting the sign.

C atom motions corresponding to the $T_{1u}(4)$ vibrational mode were taken from a complete nearest-neighbour force field model calculation for C$_{60}$, optimized to fit the optically accessible frequencies of the molecule[39]. We applied a 'frozen-phonon' approach, which assumes the Born–Oppenheimer approximation to be strictly obeyed and that the molecular orbitals adiabatically follow the atomic distortions. Although this model is not appropriate for high-frequency vibrations and low-energy electronic properties, we posit that this approach can provide the order of magnitude of the response. The t_{1u} orbitals were then computed for $T_{1u}(4)$ distorted configurations of C$_{60}$ using the Hückel model with hopping integrals varied according to equation (1). Snapshots of the driven $t_{1u}(z)$ orbital are shown in Extended Data Fig. 8b.

The Hubbard Us on each C$_{60}$ site are estimated from

$$U = F^0 = \int d^3 r_1 \int d^3 r_2 \frac{\rho(r_1)\rho(r_2)}{4\pi \epsilon_{\text{eff}} \epsilon_0 |r_1 - r_2|} \quad (2)$$

where $\rho(r)$ is the charge density corresponding to a t_{1u} orbital.

This bare U will be reduced due to screening from valence electrons, intra-molecular correlations and metallic background in a solid. However, since we

are concerned with relative changes in U this renormalization is not crucial. We estimated F^0 by assuming point charges on each C atom and calculating their mutual interactions as

$$F^0 = \sum_{i \neq j} \frac{p_i p_j e^2}{4\pi \epsilon_{\text{eff}} \epsilon_0 |r_1 - r_2|} + \sum_i p_i^2 F_C^0 \tag{3}$$

where p_i is the probability given by a t_{1u} orbital of an electron being on the ith C atom, and $F_C^0 \approx 12\,\text{eV}$ is the atomic on-site repulsion[40]. The variation of U with the vibrational driving was then obtained using the p_i values of the driven t_{1u} orbitals and is shown, together with the single-particle energies of the orbitals over a vibration period, in Extended Data Fig. 8c, d. The amplitude of the vibrational driving A denotes the maximum displacement of any C atom. For $A = 5\,\text{pm}$, both quantities in the y, z t_{1u} orbitals vary by nearly 10% at twice the frequency of the vibration.

Since the vibration is polarized along the x axis, the y, z orbitals remain degenerate and possess identical U values. The modulation in y, z is significantly larger than that in x because these orbitals have the equatorial distribution running across the vibrational axis, causing their charge distribution to compress at the poles of the x axis (Extended Data Fig. 8b).

The modulation magnitudes as a function of vibrational driving amplitude are shown in Extended Data Fig. 8e, f. An amplitude $A = 5\,\text{pm}$ is consistent with the strong vibrational driving considered in this work.

Sample size. No statistical methods were used to predetermine sample size.

27. Lupi, S. *et al.* Performance of SISSI, the infrared beamline of the ELETTRA storage ring. *J. Opt. Soc. Am. B* **24,** 959–964 (2007).

28. Plaskett, J. S. & Schatz, P. N. On the Robinson and Price (Kramers-Kronig) method of interpreting reflection data taken through a transparent window. *J. Chem. Phys.* **38,** 612–617 (1963).
29. Brito Cruz, C. H. *et al.* Dynamics of spectral hole burning. *IEEE J. Quantum Electron.* **24,** 261–269 (1988).
30. Orenstein, J. & Dodge, J. S. Terahertz time-domain spectroscopy of transient metallic and superconducting states. *Phys. Rev. B* **92,** 134507 (2015).
31. Beard, M. C., Turner, G. M. & Schmuttenmaer, C. A. Subpicosecond carrier dynamics in low-temperature grown GaAs as measured by time-resolved terahertz spectroscopy. *J. Appl. Phys.* **90,** 5915–5923 (2001).
32. Nicoletti, D., Mitrano, M., Cantaluppi, A. & Cavalleri, A. Comment on "Terahertz time-domain spectroscopy of transient metallic and superconducting states" (arXiv:1506.06758). Preprint at http://arXiv.org/abs/1506.07846 (2015).
33. Iwasa, Y. & Kaneyasu, T. Optical study of electronic structures and phonons in alkali-metal-doped C$_{60}$. *Phys. Rev. B* **51,** 3678–3685 (1995).
34. Kuzmenko, A. *et al.* Gate tunable infrared phonon anomalies in bilayer graphene. *Phys. Rev. Lett.* **103,** 116804 (2009).
35. Kresse, G. & Furthmüller, J. Efficient iterative schemes for *ab initio* total energy calculations using a plane-wave basis set. *Phys. Rev. B* **54,** 11169–11186 (1996).
36. Togo, A., Oba, F. & Tanaka, I. First-principles calculations of the ferroelastic transition between rutile-type and CaCl$_2$-type SiO$_2$ at high pressures. *Phys. Rev. B* **78,** 134106 (2008).
37. Giannozzi, P. *et al.* QUANTUM ESPRESSO: a modular and open-source software project for quantum simulations of materials. *J. Phys. Condens. Matter* **21,** 395502 (2009).
38. Laouini, N., Andersen, O. K. & Gunnarsson, O. Analytical molecular orbitals and band structures of solid C$_{60}$. *Phys. Rev. B* **51,** 17446–17478 (1995).
39. Hands, I. D., Dunn, J. L. & Bates, C. A. A complete nearest-neighbor force field model for C$_{60}$. *J. Chem. Phys.* **120,** 6912–6921 (2004).
40. Antropov, V. P., Gunnarsson, O. & Jespen, O. Coulomb integrals and model Hamiltonians for C$_{60}$. *Phys. Rev. B* **46,** 13647–13650 (1992).

a

b
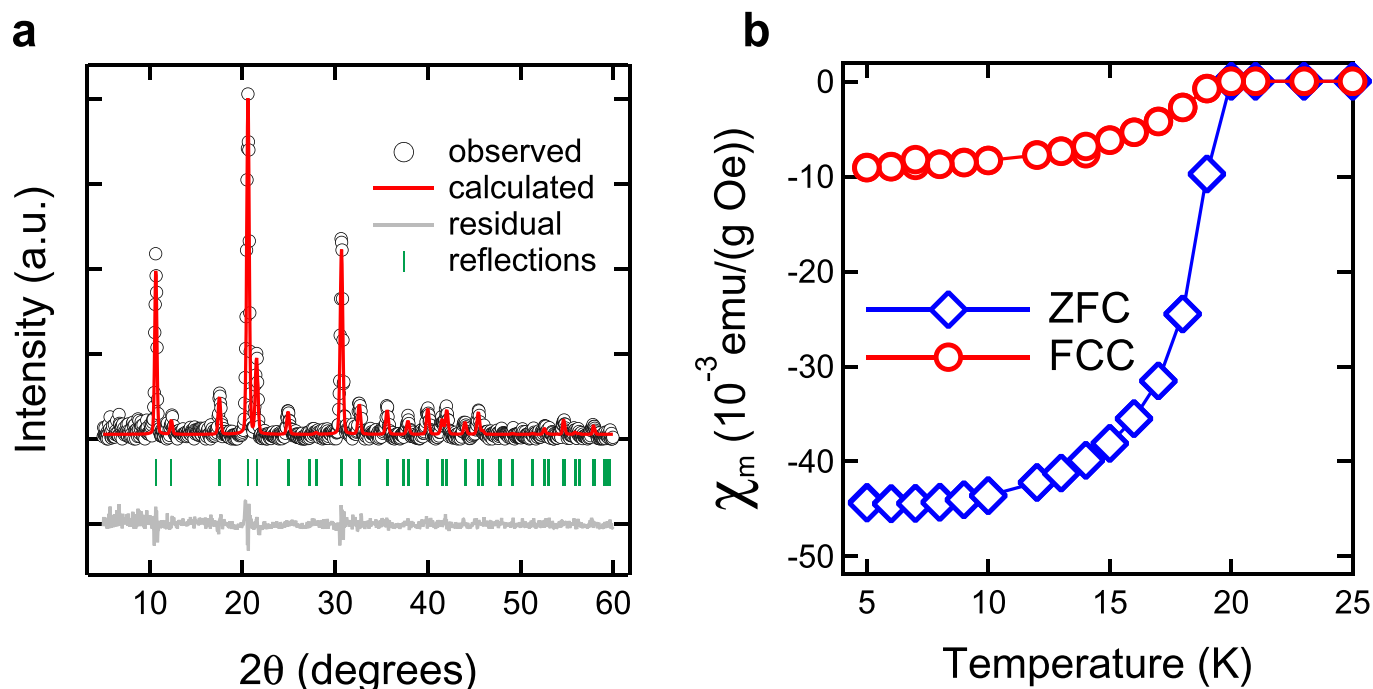
Extended Data Figure 1 | K_3C_{60} sample characterization. a, Powder X-ray diffraction of K_3C_{60} (black circles) fitted with a single f.c.c. phase Rietveld refinement (red). Positions of reflections are shown in green, fit residuals are in grey. **b**, Temperature dependent magnetic susceptibility, χ_m (FCC, field-cooled cooling; ZFC, zero-field cooling). The extracted superconducting transition temperature is $T_c = 19.8$ K.
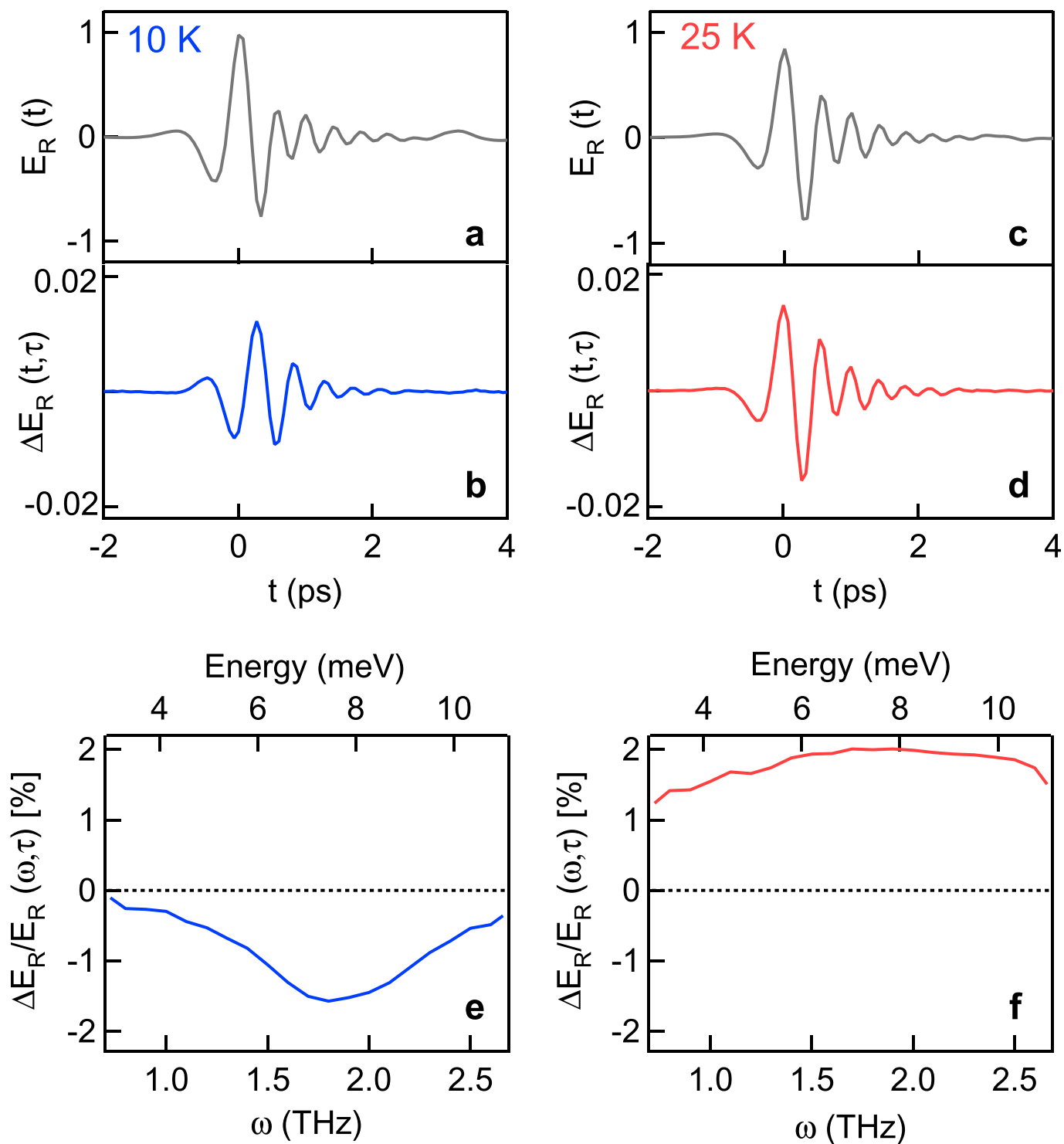
Extended Data Figure 2 | 'Raw' electric field transients below and above T_c. a–d, Stationary electric field (**a**, **c**; grey) reflected at the sample–diamond interface, $E_R(t)$, and pump-induced changes in the same quantity, $\Delta E_R(t, \tau)$, measured at $\tau = 3$ ps (**b**) and at $\tau = 1$ ps (**d**). Data are shown both below (blue) and above T_c (red). **e**, **f**, Corresponding frequency-dependent differential changes in reflectivity, $\Delta E_R/E_R(\omega, \tau)$, calculated as Fourier transform magnitude ratios of the quantities in **a–d**.
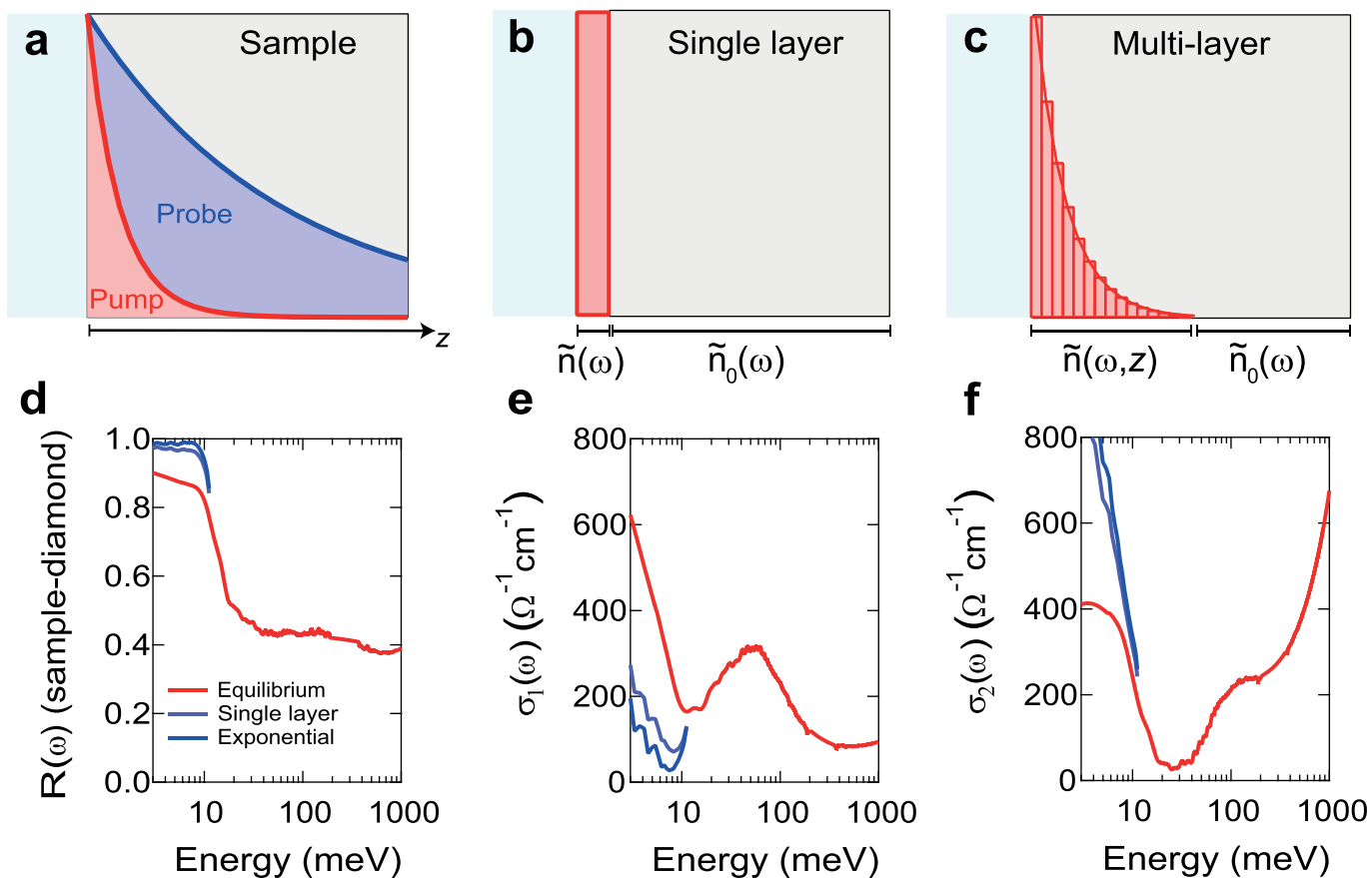
Extended Data Figure 3 | Models for penetration depth mismatch. **a**, Schematics of pump–probe penetration depth mismatch. **b**, **c**, Also shown are the single-layer model (**b**) and the multi-layer model with exponential decay (**c**) (see Methods) used to calculate the pump-induced changes in the complex refractive index, $\tilde{n}(\omega)$. **d**–**f**, Reflectivity, $R(\omega)$, and complex optical conductivity, $\sigma(\omega)$, of K_3C_{60} at $\tau = 1\,ps$ pump–probe delay and $T = 25\,K$, extracted using the single-layer model (light blue) and the multi-layer model with exponential decay (dark blue).
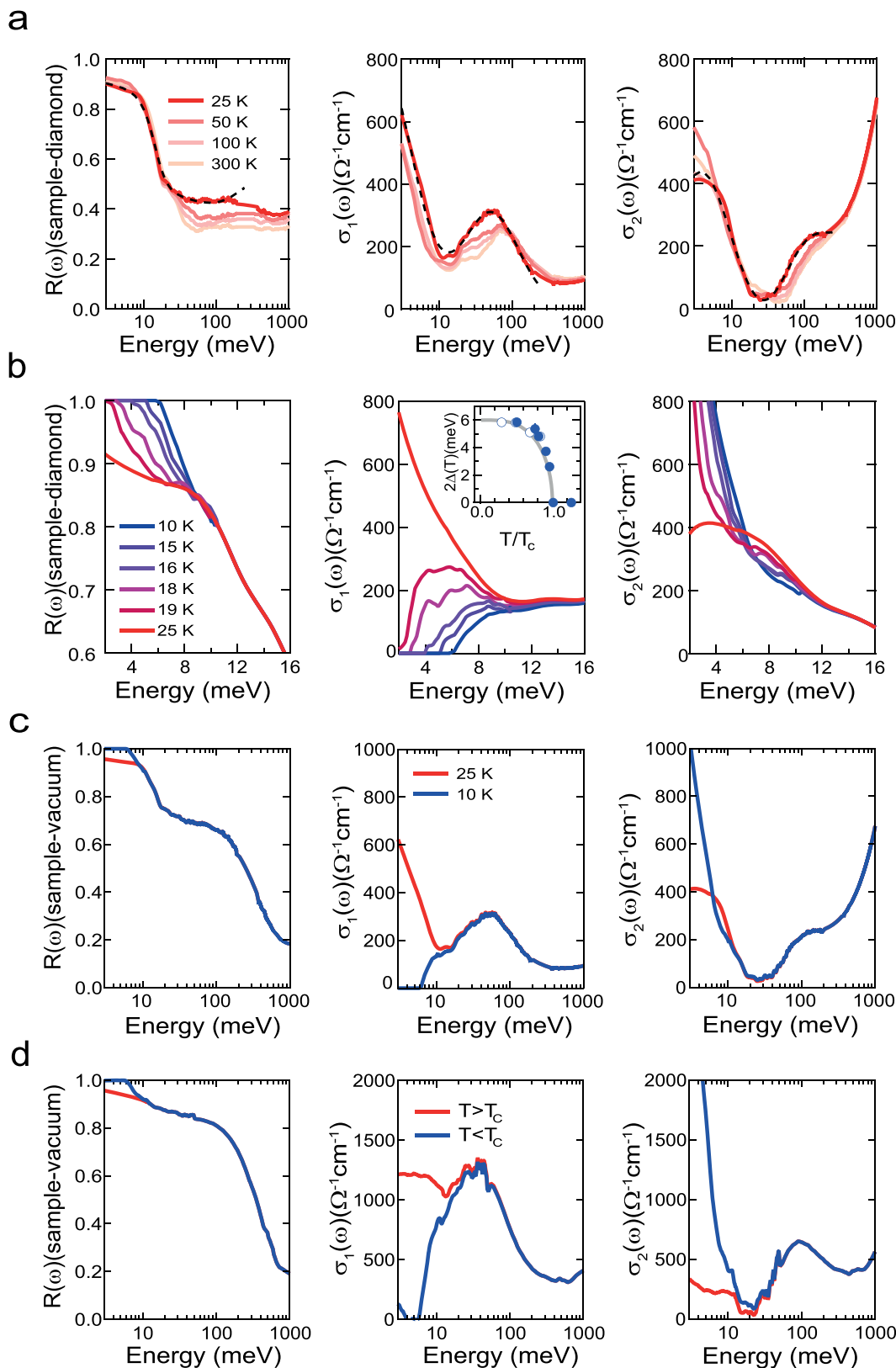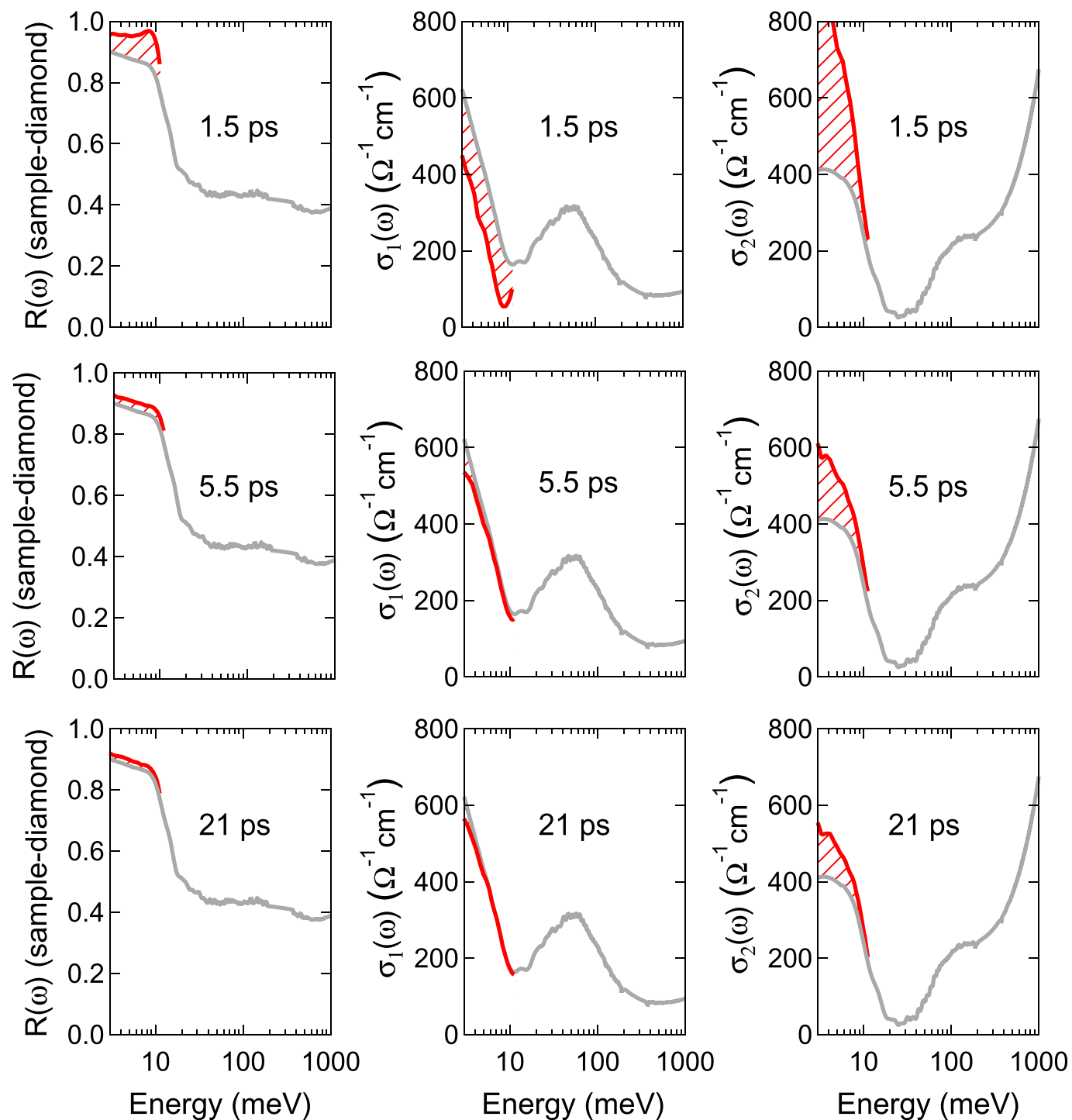
Extended Data Figure 4 | Equilibrium optical properties. a, Reflectivity (left column), and real and imaginary parts (respectively middle and right columns) of the optical conductivity of K_3C_{60} displayed at different temperatures above T_c. Dashed lines are fits to the 25 K data performed with a Drude–Lorentz model. **b**, Same quantities displayed at different $T < T_c$. In the inset, the temperature dependent optical gap (filled circles) is compared with previously published data on K_3C_{60} single crystals (open circles[18]). **c**, Optical properties of compressed powders of K_3C_{60} from **a** and **b** shown at representative temperatures below and above T_c. The $R(\omega)$ has been recalculated at the sample–vacuum interface. **d**, Same quantities as in **c**, measured on single crystals[18].
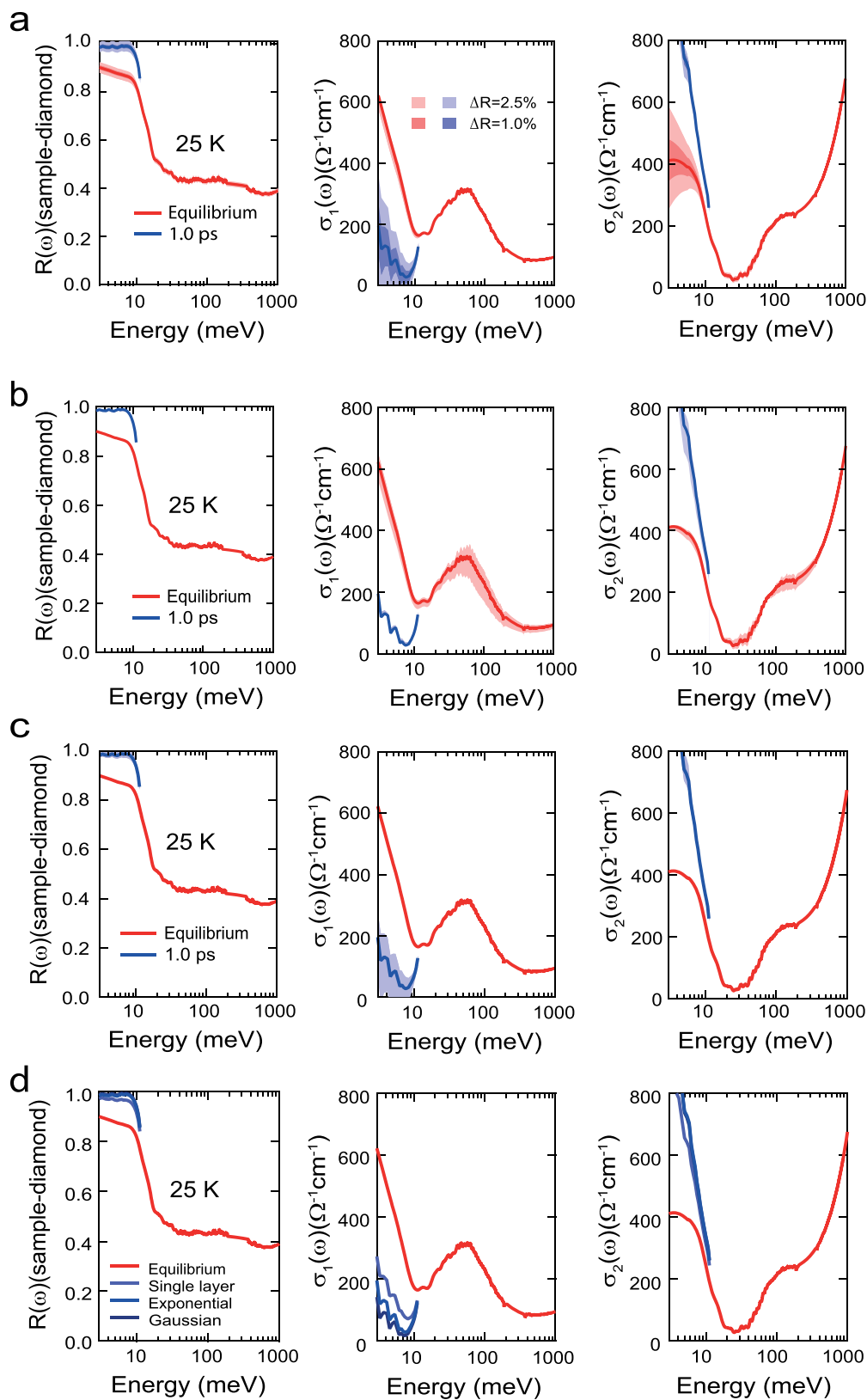
Extended Data Figure 5 | Uncertainties in determining the transient optical properties. Columns as Extended Data Fig. 4; shown are values for K_3C_{60} at equilibrium (red) and 1 ps after photo-excitation (blue) at $T = 25$ K. Error bars, displayed as coloured bands, have been propagated as follows: **a**, $\pm 1\%$ and $\pm 2.5\%$ uncertainty in the equilibrium $R(\omega)$; **b**, $\pm 10\%$ uncertainty in the equilibrium Fresnel phase coefficient β (see Methods);

c, $\pm 25\%$ change in the pump penetration depth $d = 220$ nm. In **d** we analyse the effect of different functional forms for modelling the pump–probe penetration depth mismatch (see Methods): a single-layer model, or a multi-layer model with exponential decay or with Gaussian-like decay, all with the same pump penetration depth $d = 220$ nm.

Extended Data Figure 6 | Relaxation dynamics at $T > T_c$. Reflectivity (left column) and complex optical conductivity (middle and right columns) of K_3C_{60} at equilibrium (grey) and after photo-excitation (red) at $T = 25$ K. Data have been measured with a pump fluence of ~1 mJ cm^{-2} and are shown at selected pump–probe time delays: 1.5 ps, 5.5 ps and 21 ps (top, middle and bottom rows, respectively). Hatched areas highlight pump-induced changes.

a

b

c

d
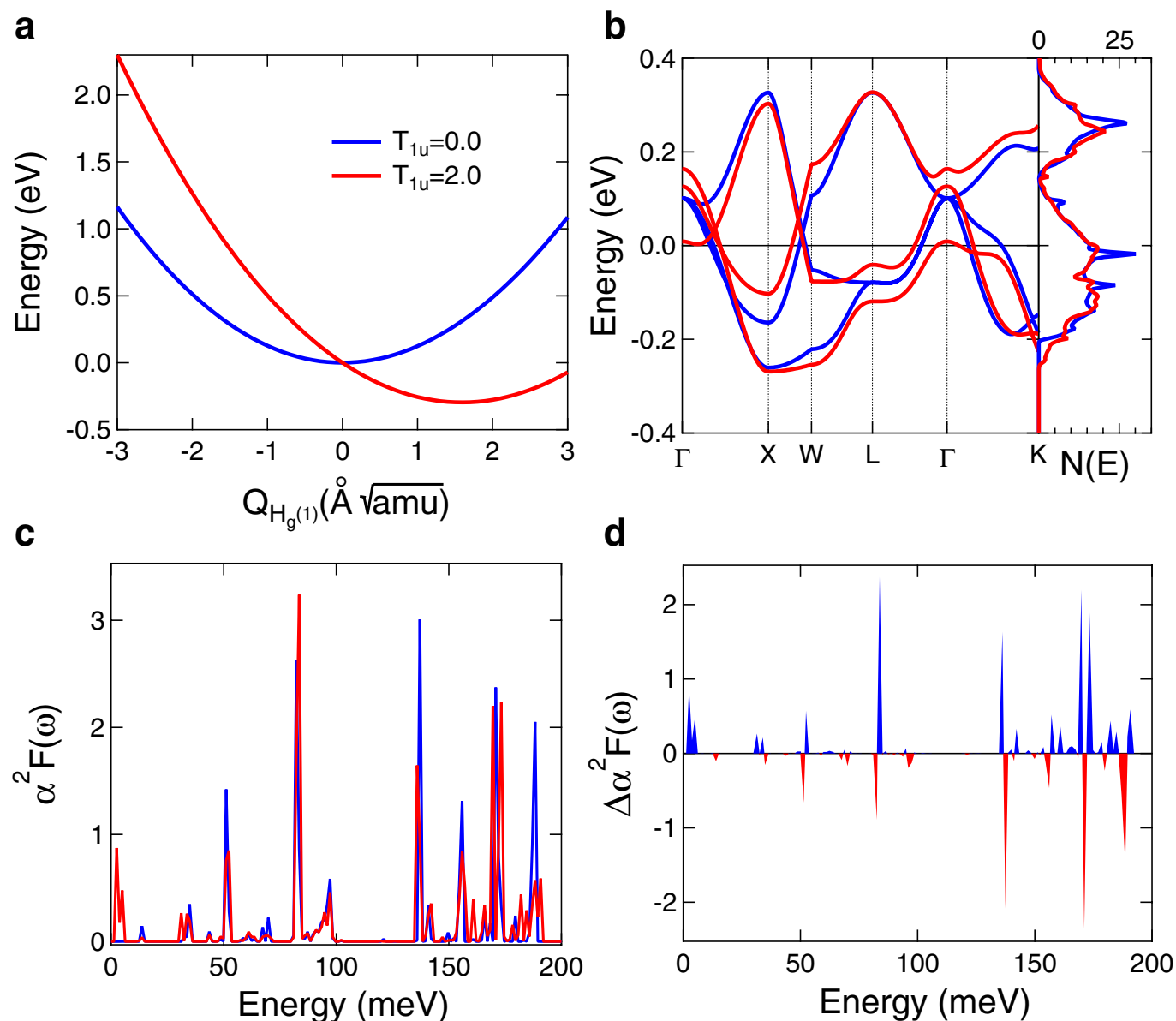
Extended Data Figure 7 | Mode coupling and electronic structure calculations. a, Calculated total energy curves as a function of $H_g(1)$ mode amplitude ($Q_{H_g(1)}$) when the amplitude of the $T_{1u}(4)$ mode is 0.0 (blue) and 2.0 Å √amu (red). **b**, Calculated band structure and electronic density of states $N(E)$ of K_3C_{60}. **c**, Calculated electron–phonon coupling function, $\alpha^2 F(\omega)$. In **b** and **c**, blue lines are for the equilibrium structure and red lines are for the structure displaced along the $H_g(1)$ coordinate with an amplitude of 1.5 Å √amu. **d**, Differential changes in the electron–phonon coupling function, evaluated from the curves in **c**.
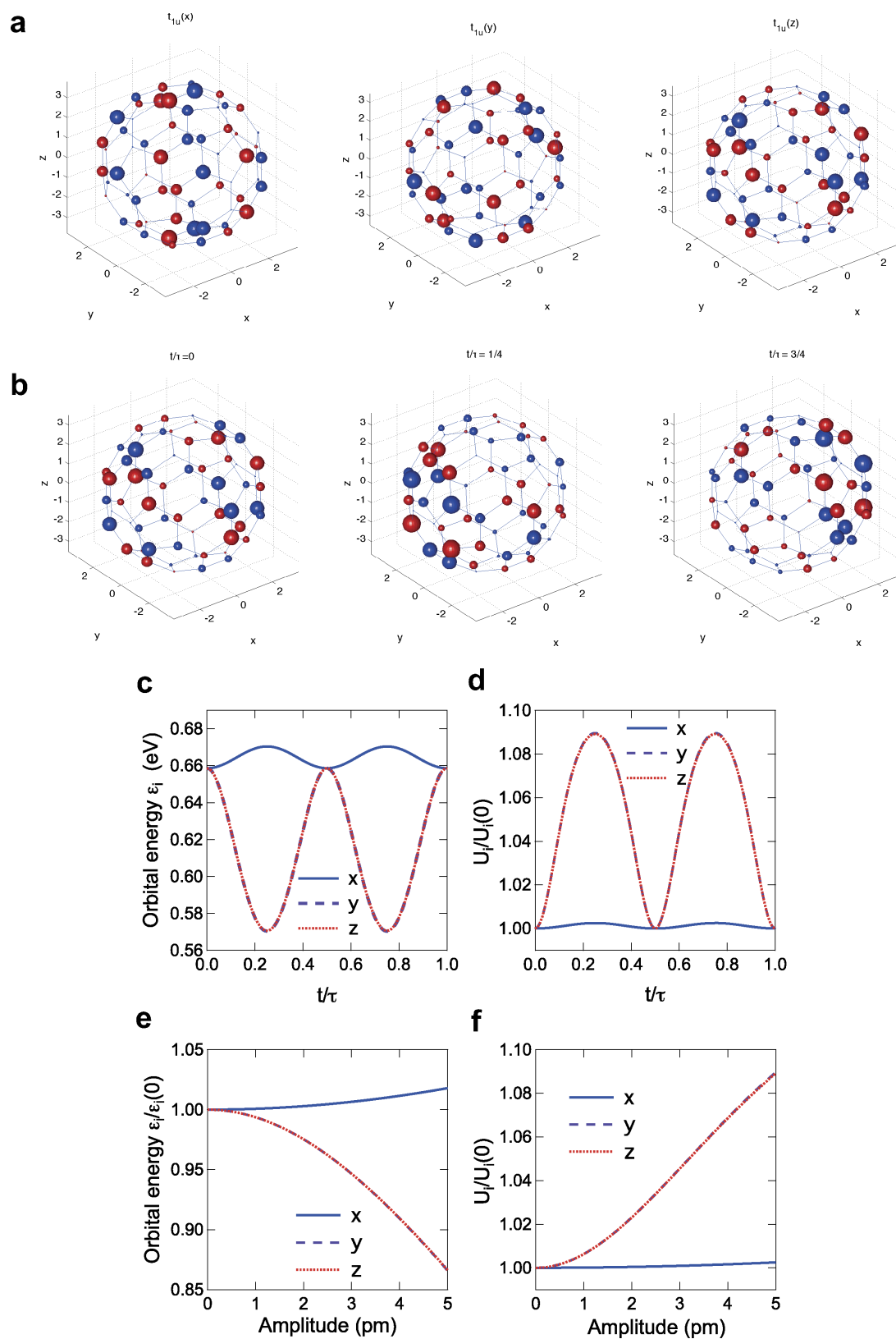
Extended Data Figure 8 | Changes in time of single particle energy and Coulomb repulsion. a, Depiction of the x, y, z t_{1u} orbital wavefunctions of C_{60} according to the Hückel model (left, middle and right column respectively, see Methods). Sphere sizes denote the magnitude of the wavefunction and colours indicate the sign. **b**, Snapshots of the calculated $t_{1u}(z)$ orbital at various points in the $T_{1u}(4)$ vibration polarized along the x axis. Colours and sizes follow those of **a**. **c**, Changes in the single-particle energies, ε_i, of the t_{1u} orbitals over one period of the $T_{1u}(4)$ vibration with an amplitude $A = 5$ pm. **d**, Relative changes in the intra-orbital Coulomb repulsions, $U_i/U_i(0)$. **e**, Maximum relative changes in the single-particle energies of the t_{1u} orbitals, $\varepsilon_i/\varepsilon_i(0)$, as a function the driving amplitude, A. **f**, Relative changes in the intra-orbital Coulomb repulsions, $U_i/U_i(0)$, under the same driving conditions.
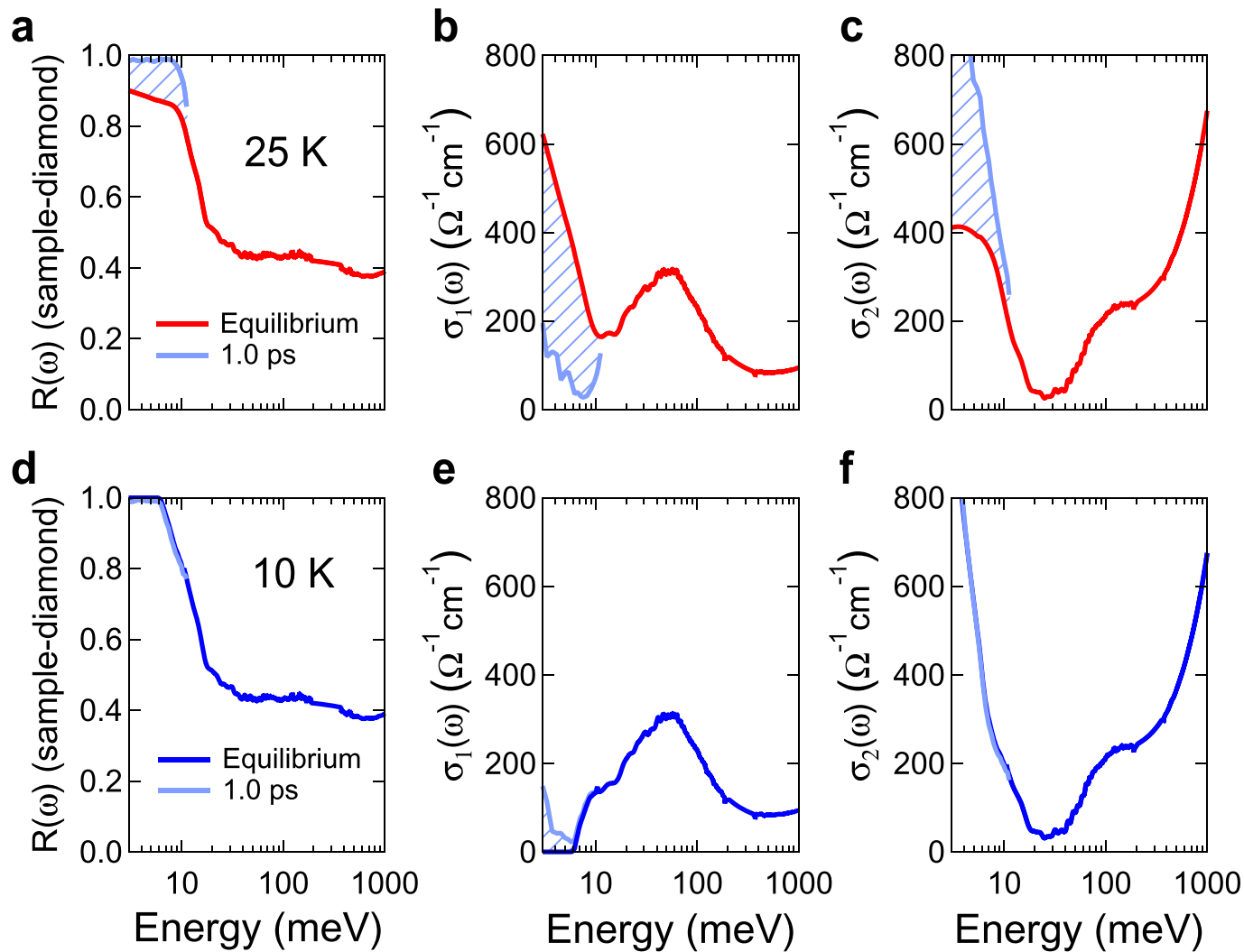
Extended Data Figure 9 | Response at early time delays below and above T_c. Reflectivity, $R(\omega)$, and complex optical conductivity, $\sigma(\omega)$, of K_3C_{60} at equilibrium (red, dark blue) and 1 ps after photo-excitation (light blue), measured at $T > T_c$ (**a–c**) and $T < T_c$ (**d–f**). Data were taken using pump fluences of ~ 1 mJ cm^{-2} in **a–c** and ~ 0.5 mJ cm^{-2} in **d–f**. Hatched areas highlight pump-induced changes.
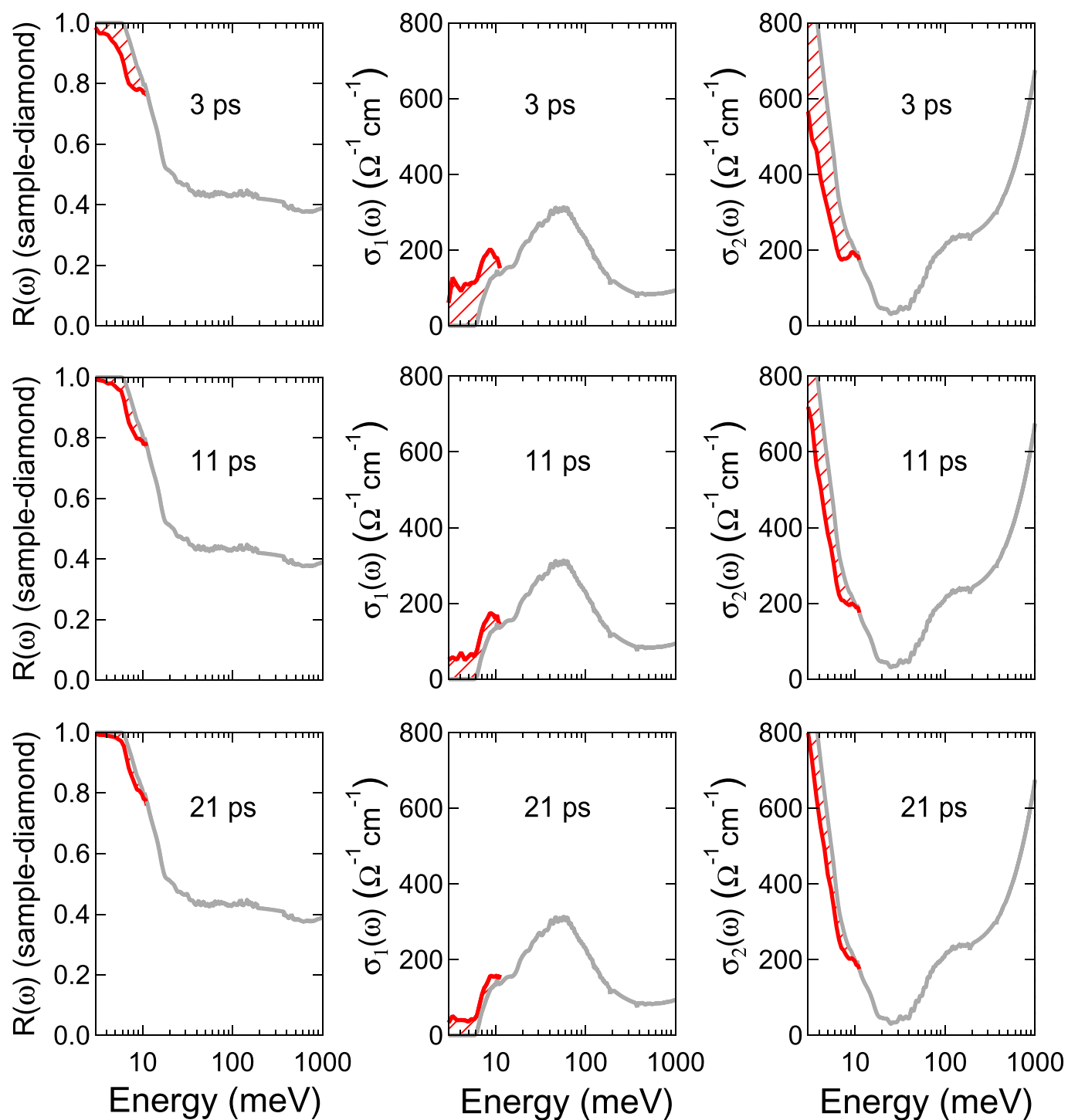
Extended Data Figure 10 | Relaxation dynamics at $T < T_c$. Columns as Extended Data Fig. 9; data were measured at equilibrium (grey) and after photo-excitation (red) at $T = 10$ K, with a pump fluence of ~0.5 mJ cm^{-2}. Data are shown at selected pump–probe time delays: 3 ps (top row), 11 ps (middle row) and 21 ps (bottom row). Hatched areas highlight pump-induced changes.